Applied Catalysis B: Environmental 312 (2022) 121418

Contents lists available at ScienceDirect

Applied Catalysis B: Environmental

journal homepage: www.elsevier.com/locate/apcatb

Efficient degradation of sulfamethazine in a silicified microscale zero-valent iron activated persulfate process

Minda Yu [a,b,c], Xuhui Mao [b], Xiaosong He [a,c], Mingxia Zheng [a,c], Xu Zhang [a,c], Jing Su [a,c], Beidou Xi [a,c,*]

[a] State Key Laboratory of Environmental Criteria and Risk Assessment, Chinese Research Academy of Environmental Sciences, China
[b] School of Resources and Environmental Science, Hubei International Scientific and Technological Cooperation Base of Sustainable Resource and Energy, Wuhan University, Wuhan 430079, China
[c] State Environmental Protection Key Laboratory of Simulation and Control of Groundwater Pollution, Chinese Research Academy of Environmental Sciences, China

ARTICLE INFO

Keywords:
Mechanical silicification
Microscale zero-valent iron
Reactive species
High-valent iron
Iron cycle

ABSTRACT

Microscale zero-valent iron (mZVI) is used as a catalyst for peroxide activation and, has attracted considerable attention for the degradation of organic contaminants. However, surface inherent oxide films impedes electron transfer in mZVI and decrease its activation efficiency. Herein, the mZVI surface was modified by sodium disilicate (Si-mZVI^{bm}) using a mechanical ball-milling approach. The mechanochemically silicified mZVI enhanced the sulfamethazine removal rate by 2.9–23.8 fold in relation to unmodified ZVI; this rate increased with the Si/Fe molar ratio (0–8%). Reactive intermediates, including radicals and non-radicals, were efficiently generated via peroxydisulfate (PDS) activation over Si-mZVI^{bm} both $SO_4^{\bullet-}$ and Fe(IV) contributed toward sulfamethazine removal. The excellent performance of PDS activation over Si-mZVI^{bm} particles was attributed to the continuous generation of ferrous ions, which was due to the accelerated iron release and more effective Fe^{3+}/Fe^{2+} cycles in the Si-mZVI^{bm}/PDS system after silicification.

1. Introduction

The presence of pharmaceutical residues, especially antibiotics, in the ecosystem is considered a crucial global environmental concern. Sulfamethazine (SMT), which is a typical sulfonamide antibiotic, is extensively used in human and veterinary medicine [1,2]. However, this drug is mostly released into the environment; thus, it is frequently detected in various environmental media [3,4]. Additionally, the presence of antibiotics promotes the dissemination of antibiotic resistant genes and reduces the resistance to bacterial pathogens, thereby posing a significant threat to the ecosystem and human health [4,5]. Therefore, it is crucial to exploit an efficient technology to remediate these issues.

Chemical oxidation utilizing activated peroxydisulfate (PDS; $S_2O_8^{2-}$) is a promising method for the removal of bio-recalcitrant organic contaminants. Generally, PDS can be activated by the cleavage of the peroxide bond, generating strong reactive intermediates, such as sulfate radicals ($SO_4^{\bullet-}$), hydroxyl radicals (•OH), superoxide radicals ($O_2^{\bullet-}$), and high-valent iron species (Fe(IV)) [6–9]. Additionally, iron-based materials, in particular zero-valent iron (ZVI), have been used for PDS activation owing to their high activation efficiency, low cost, and environmental friendliness [10–12]. ZVI can continuously replenish Fe^{2+} ions to activate PDS, and it can directly transfer electrons to PDS for the generation of $SO_4^{\bullet-}$. ZVI can also regenerate Fe^{2+} from Fe^{3+} formed through PDS activation [13–15]. Unfortunately, an intrinsic passivation layer may be formed during the storage and use of ZVI, restricting electron transfer and Fe^{2+} regeneration. The PDS activation efficiency and longevity of ZVI further decrease with the accumulation of passive oxides on the ZVI surface.

Various methods to enhanced the ZVI activity have been reported, which include removing, destroying, and replacing the passive oxide layer by chemical and/or physical processes. ZVI activity was enhanced by removing the oxide layer through acid washing and re-reduction; however, its recovery activity rapidly decreased again with the regeneration of the iron oxide layer [16–18]. Replacing iron oxides with iron sulfide or iron phosphate has recently been considered a promising alternative. The formation of the resulting sulfur- and phosphorus-containing oxide layer, increases the electron conductivity, selectivity, and depassivation efficiency of the iron surface [19–21].

* Corresponding author at: State Key Laboratory of Environmental Criteria and Risk Assessment, Chinese Research Academy of Environmental Sciences, China.
E-mail addresses: BDXI21@yeah.net, xibd@craes.org.cn (B. Xi).

https://doi.org/10.1016/j.apcatb.2022.121418
Received 10 February 2022; Received in revised form 2 April 2022; Accepted 13 April 2022
Available online 20 April 2022

These approaches can improve the reactivity of ZVI; however, its application is limited by the associated high cost and pollution potential. Therefore, it is crucial to develop methods based on low-cost and sustainable (i.e., "green") processes.

Mechanochemical surface functionalization has emerged as one of the most promising, cost-effective, and environmentally friendly method for preparing high-activity ZVI-based materials (such as sulfidated ZVI, bimetallic ZVI, and Fe-C composites) [22–24]. The mechanical force during the milling process can deform the ZVI shape, fracture the oxide layer, and expose the iron core. Consequently, ball-milled ZVI ($mZVI^{bm}$) is considered to be more effective for PDS activation than bare ZVI. Additionally, mechanochemical functionalization is used for surface modification because different materials will undergo a solid-solid reaction, thereby yielding novel characteristics to the product [25,26]. For decades, dissolved silicate has been used as a non-toxic and eco-friendly iron corrosion inhibitor and ligand [27,28]. Silicate can easily cover the film surface of iron/iron oxides; thus, the formed inhibition film can affect the iron oxide reactivity. Previous studies indicated that silicate inhibition films could affect the activity of iron catalysts toward the H_2O_2-based oxidation process by inhibiting H_2O_2 decomposition and lowering H_2O_2 utilization efficiency [29]. Conversely, silicate inhibition films efficiently catalyst the decomposition of ozone and inhibit the excessive corrosion of iron [30]. We recently reported that silicate can act as a ligand to modify the dissolution and redox properties of iron, thereby enhancing the removal of organic pollutants [31,32]. Accordingly, silicate compounds and their preparation methods have disparate effects on the activity of iron-based catalysts reactivity. Additionally, understanding the structure reactivity relationship of the silicate-coated iron oxides surface is crucial to optimize and design iron-based catalysts. To the best of our knowledge, the applicability of modified ZVI by mechanical silicification as a catalyst for PDS activation has not been verified, and the underlying mechanisms of silicification in the PDS activation have not been explored.

In this study, microscale ZVI particles containing silicate compounds ($Si\text{-}mZVI^{bm}$) were synthesized by ball milling ZVI and disilicate powders under dry conditions. Additionally, the effects of the mechanical silicification treatment on the structural changes and the SMT degradation efficiency of the $Si\text{-}mZVI^{bm}$ catalyst were investigated by the activated PDS oxidation process. We interestingly found the mechanical silicification of mZVI facilitated the activation of PDS by efficient electron transfer and Fe^{3+}/Fe^{2+} cycles. We believe that this work will help in understanding the effects of silicate modification on the catalytic reaction of iron-based persulfate process and will provide high-efficiency ZVI-based technologies for water remediation.

2. Materials and methods

2.1. Chemicals and materials

Sodium persulfate ($Na_2S_2O_8$) was purchased from Sinopharm Chemical Reagent Co., Ltd. Commercial mZVI powder (100 mesh, >99% purity) was purchased from Alfa-Aesar Company. Sodium disilicate ($Na_2Si_2O_5$; purity >95% purity) was purchased from Yousuo Chemical Technology Co. (China). Sulfamethazine (SMT) ($C_{12}H_{14}N_4O_2S$; 99% purity) was obtained from Aladdin Industrial Cooperation, China. Methyl phenyl sulfoxide (PMSO) and methyl phenyl sulfone ($PMSO_2$) were purchased from Sigma-Aldrich. All other chemicals were of analytical grade and used without further purification. Deionized water was used for all experiments.

2.2. Preparation of silicified microscale zero-valent iron

To prepare $Si\text{-}mZVI^{bm}$, mZVI and sodium disilicate powder were mixed and sealed in a jar (100 mL) with a little oxygen headspace. Milling was then performed using a planetary ball mill operated at 550 rpm for 4 h. The weight ratio of steel balls to mixed powder was 35.7:1, and the Si/Fe molar ratio was 0.01–0.08. For comparison, commercial mZVI powder was ball-milled under the same conditions without adding sodium disilicate (denoted as $mZVI^{bm}$).

2.3. Batch experiment procedure

Batch experiments were performed in a 250 mL flask opened under an air atmosphere at room temperature (20 ± 5 °C). The experiments were conducted after the addition of desired amounts of oxidant (PDS) and catalyst ($Si\text{-}mZVI^{bm}$, $mZVI^{bm}$, or mZVI) to a 150 mL SMT stock solution (10 mg/L) without a buffer, followed by mechanically stirring at 250 rpm. H_2SO_4 and NaOH were added to adjust the pH of the solution, if necessary. During the reaction, 1 mL of the sample was withdrawn at different intervals and immediately quenched with excess ethanol (EtOH). The reactive species were identified using different quenching agents, including EtOH, tertiary butanol (TBA), furfuryl alcohol (FFA), and trichloromethane ($CHCl_3$). The PMSO degradation experiment was conducted to determine the role of Fe(IV) [33]. The effects of experimental factors, such as the Si/Fe molar ratio, $Si\text{-}mZVI^{bm}$ dosage, PDS dosage, initial pH, and inorganic ions, were investigated by changing the parameters accordingly. All batch experiments were conducted in duplicate or triplicate to ensure the achievement of highly accurate results.

2.4. Analytical methods

The concentrations of SMT, PMSO, and $PMSO_2$ were analysed using a high-performance liquid chromatography equipped with an UV detector. SMT degradation intermediates were identified through high-performance liquid chromatography-tandem mass spectrometry (HPLC-MS); the details of this analysis are provided in the Supporting Material (SM; Tests S1–S2). The concentrations of Fe^{2+} and total iron were measured using the phenanthroline method. The radical species were determined using an electron paramagnetic resonance (EPR) instrument (Micro EPR, Bruker, Germany). Electrochemical characterization was performed using an electrochemical workstation (CHI-760E, China) with a three-electrode system. The detailed morphology, elemental composition of the materials, and competition kinetics experiment are described in the SM (Tests S3–S5).

3. Results and discussion

3.1. Promoting effect of silicification on PDS activation by $mZVI^{bm}$

The surface morphology and elemental composition of $mZVI^{bm}$ and $Si\text{-}mZVI^{bm}$ were investigated through scanning electron microscopy equipped with energy dispersive X-ray (SEM-EDX). Fig. S1 shows that the shape of ZVI was broken and pressed after milling. The surface morphology became rough when disilicate was added during milling, and some irregular particles aggregated on the surface. The specific surface area of the $mZVI^{bm}$ particles increased from 0.35 to 2.04 m^2 g^{-1} after the silicification treatment (Fig. S2). Bare $mZVI^{bm}$ was free of silicon (Fig. S3) and $Si\text{-}mZVI^{bm}$ contained Fe, Si, and O (Fig. 1(a–d)), suggesting that Si was introduced during the silicification treatment. X-ray diffraction (XRD) patterns did not show peaks for any new silicon-bearing compounds (Fig. S4), indicating that silicon content or crystallinity degree was low. The X-ray photoelectron spectroscopy (XPS) revealed that silicon was only present on the surface of $Si\text{-}mZVI^{bm}$ (Fig. 1 (e) and S5(a)). The silicon peak in the XPS spectra of $Si\text{-}mZVI^{bm}$ continued to exist with the increase in etching time (Fig. S5(b)), further confirming that silicon was loaded on the surface of $Si\text{-}mZVI^{bm}$. Moreover, the high-resolution Si 2p and Fe 2p peaks shifted to a lower binding energy after ball milling with disilicate (Fig. S5(c)), implying that the introduction of silicon led to a change in the oxidation state on $Si\text{-}mZVI^{bm}$. Oxygen from iron oxides (530.0 eV) and iron hydroxides (531.3 eV) were detected in both the O 1 s XPS spectra of $mZVI^{bm}$ and Si-

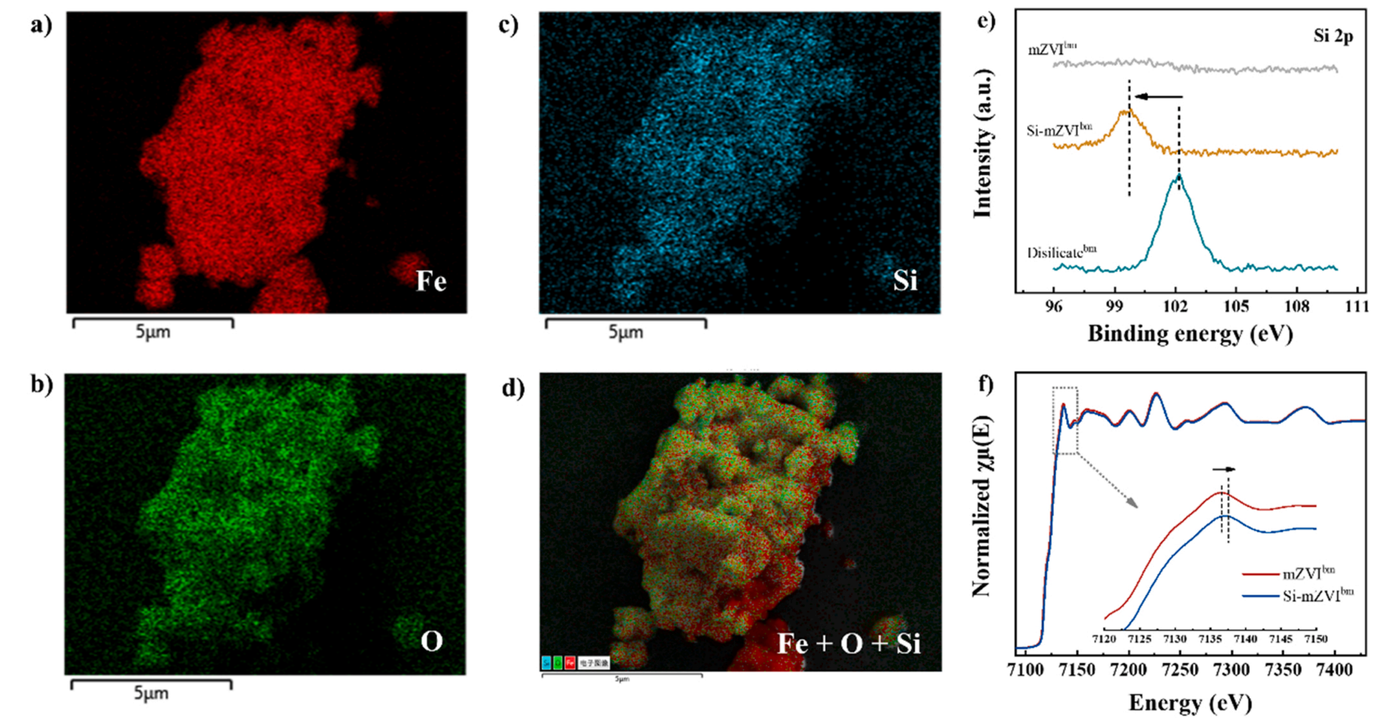

Fig. 1. Morphology and component analysis of $mZVI^{bm}$ and Si-$mZVI^{bm}$ with Si/Fe = 0.04. (a-d) SEM-EDX elemental mapping of Fe, Si, O, and their overlapped images. (e) High-resolution XPS Si 2p spectra of $disilicate^{bm}$, $mZVI^{bm}$ and Si-$mZVI^{bm}$. (f) Fe K-edge X-ray absorption near-edge structure (XANES) spectra of $mZVI^{bm}$ and Si-$mZVI^{bm}$.$Disilicate^{bm}$ in (e) is pure ball-milled sodium disilicate.

$mZVI^{bm}$ (Fig. S5(d)). Ball milling decreased the molar fractions of iron hydroxides from 70% to 60.0%, indicating the partial replacement of surface hydroxyls by silicate groups. Fourier transform infrared spectra showed the characteristic bands of Si-OH, Si-O-Si, and Fe-O-Si at approximately 1070, 638, and 470 cm^{-1}, respectively (Fig. S6), confirming the presence of Fe-O-Si bonds on the Si-$mZVI^{bm}$ surface.

X-ray absorption fine structure spectroscopy was conducted to clarify the local atomic arrangement of $mZVI^{bm}$ and Si-$mZVI^{bm}$. The X-ray absorption near-edge spectra (Fig. 1(f)) show that the maximum intensity of the Fe K-edge spectral peak of Si-$mZVI^{bm}$ was higher than that of $mZVI^{bm}$. Additionally, a slight reduction in the Fe K-edge oscillation was noted for Si-$mZVI^{bm}$ in relation to that for $mZVI^{bm}$ (Fig. S7), confirming the structural difference in the coordination environment surrounding the Fe atoms. These abovementioned results confirmed the introduction of silicate on the Si-$mZVI^{bm}$ surface through the mechanochemical silicification treatment of mZVI, which would inevitably affect the reactivity of mZVI.

The SMT removal efficiencies of $mZVI^{bm}$, Si-$mZVI^{bm}$, PDS, $mZVI^{bm}$/PDS, and Si-$mZVI^{bm}$/PDS were investigated. Fig. 2(a) suggest that no apparent SMT degradation was observed during the control experiments when only $mZVI^{bm}$, Si-$mZVI^{bm}$, and PDS were used. However, SMT degradation efficiency reached 17.5% and 95.2% in $mZVI^{bm}$/PDS and Si-$mZVI^{bm}$/PDS, respectively. The silicification treatment improved the SMT degradation rate of PDS activation by $mZVI^{bm}$, and the pseudo-first-order reaction rate constant (k_{obs}, min^{-1}) of SMT degradation increased from 0.0078 ($mZVI^{bm}$/PDS) to 0.089 min^{-1} (Si-$mZVI^{bm}$/PDS) (Fig. S8). When the Si/Fe molar ratio increased from 1% to 8%, the promotional effect improved further (Fig. 2(b)). Impressively, for sulfonamide antibiotics removal in the iron-based persulfate activation systems, performance of Si-$mZVI^{bm}$ surpassed the most of the reported iron-based catalysts (Table S1). Subsequently, the reusability of the Si-$mZVI^{bm}$ activation of PDS for SMT degradation was evaluated (Fig. 2(c)). The SMT degradation efficiency in Si-$mZVI^{bm}$/PDS decreased slightly when Si-$mZVI^{bm}$ was used over four cycles, whereas the SMT removal rate in Si-$mZVI^{bm}$/PDS remained at 68.4% under the same reaction time. Thus, mechanical silicification is considered a promising strategy to improve the mZVI activation of PDS for SMT degradation. To better understand the enhancement in the degradation mechanism and identify the reactive species in PDS-based systems, 4% Si-$mZVI^{bm}$ was chosen for further experiments.

3.2. Identification of reactive species involved in Si-$mZVI^{bm}$/PDS

Reactive species, containing radicals and non-radicals, are generated in the iron-based heterogeneous activation of PDS [15]. To identify the existence and dominant reactive species for SMT degradation in the Si-$mZVI^{bm}$/PDS process, EPR tests, scavenger quenching experiments, and the conversion of PMSO to $PMSO_2$ Si-$mZVI^{bm}$/PDS system were evaluated.

EPR was used with DMPO as the trapping agent to examine the free radical species. Fig. 3(a) shows that DMPO-SO_4^- (six lines, 1:1:1:1:1:1, with hyperfine splitting constants (hfsc) of $\alpha_N = 13.2$ G and $\alpha_H = 9.6$ G) and DMPO-OH (four lines, 1:2:2:1, with hfsc of $\alpha_N = \alpha_H = 14.9$ G) signals were captured, confirming the existence of $SO_4^{\bullet-}$ and •OH radicals in the Si-$mZVI^{bm}$/PDS system [34,35]. Following the identification of the free radical species, scavenger quenching experiments were conducted to evaluate their contribution to the degradation. Ethanol can efficiently quench both $SO_4^{\bullet-}$ and •OH, while TBA is a more effective quenching agent for •OH [36,37]. Additionally, FFA and $CHCl_3$ were selected to quench $^1O_2$ and $O_2^{\bullet-}$, respectively [31,38]. The slight inhibition effect of FFA and $CHCl_3$ on SMT degradation suggests that $^1O_2$ and $O_2^{\bullet-}$-mediated oxidation process was less responsible for SMT degradation (Fig. 3(b)). The presence of EtOH and TBA reduced the SMT removal efficiencies from 94.3% to 7.9% and 83.6%, respectively. These results demonstrated that both •OH and $SO_4^{\bullet-}$ were the reactive radical species in Si-$mZVI^{bm}$/PDS system, and that $SO_4^{\bullet-}$ played the dominant role, because EtOH exhibited a higher inhibition effect on SMT degradation than TBA.

The EPR and quenching test results only clarified the free radical signals; however, non-radical pathways (e.g. Fe(IV)) might exist in the Si-$mZVI^{bm}$/PDS system. Furthermore, DMPO-OH adducts were

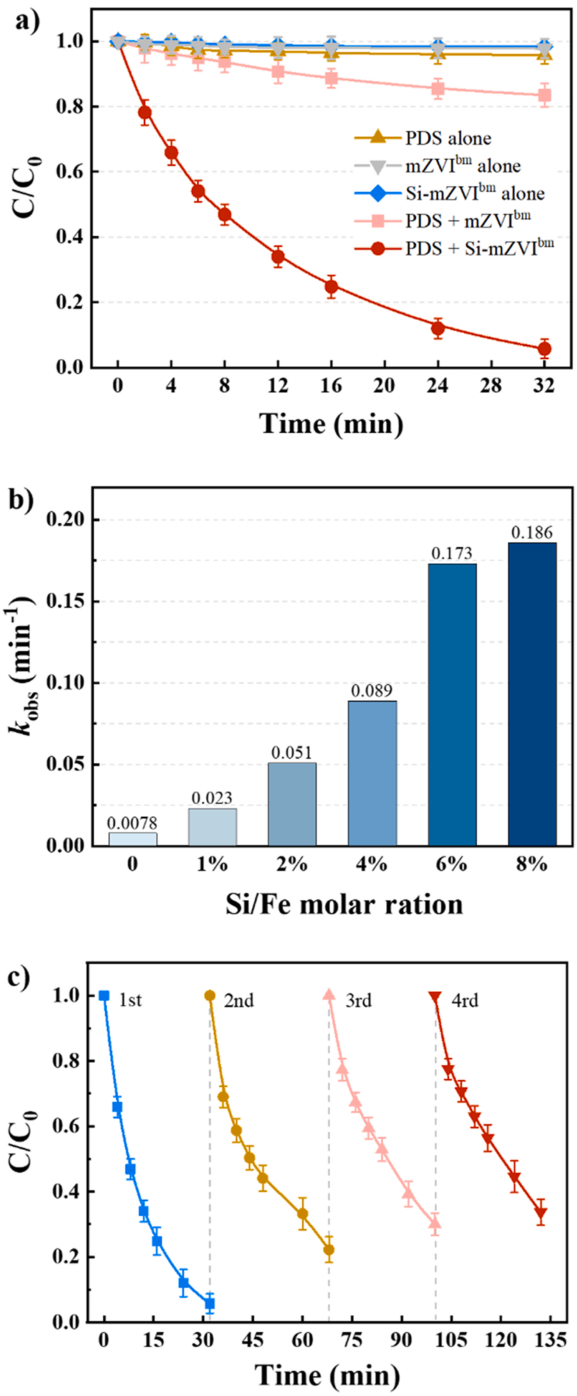

Fig. 2. (a) Removal of SMT in different systems. (b) The corresponding kinetic constants of the Si-mZVI^{bm}/PDS system under different Si/Fe molar ratios. (c) Reusability of Si-mZVI^{bm} activation of PDS in SMT degradation. Experimental conditions: 10 mg/L SMT, 0.15 g/L Si-mZVI^{bm}, and 1.5 mM PDS and initial pH 7.5.

generated by the direct oxidation of Fe(IV), EtOH can quench the generated Fe(IV) [8,39], possibly leading to an over-exaggeration of the free radical contributions in the system. To elucidate the existence of Fe (IV), PMSO was chosen as the probe compound because it can selectively produce $PMSO_2$ through oxygen transfer with Fe(IV). As shown in Fig. 3 (c), the loss of PMSO by Si-mZVI^{bm}/PDS system at an initial pH of 7.5 increased as the reaction proceeded, with $PMSO_2$ being formed gradually and its maximum production value reaching 67.4 μM at 32 min. Moreover, the $PMSO_2$ yield (that is, $\eta(PMSO_2) = 67.2\%$) and the molar ratio of $PMSO_2$ to PMSO depletion, was calculated to evaluate the contribution of Fe(IV) to PMSO degradation. To explore the role of Fe (IV) in the degradation of SMT, the effects of phenol and amoxicillin (Amoxi) on SMT removal were investigated. Because phenol and Amoxi contain electron-rich or thioether moieties, they are easily selectively oxidized by Fe(IV) [40], thereby weakening the SMT degradation effect of Fe(IV) in the Si-mZVI^{bm}/PDS system. As expected, SMT removal was suppressed by 41.4% and 47.9% in the presence of Amoxi and phenol, respectively (Fig. 3(d)), suggesting that Fe(IV) was produced in the Si-mZVI^{bm}/PDS system and it played a crucial role in SMT degradation.

Based on the EPR, scavenger quenching, and PMSO probe experiment results, we concluded that Fe(IV), •OH, and $SO_4^{\bullet-}$ were responsible for SMT degradation in the Si-mZVI^{bm}/PDS system. Competition kinetics experiment were performed using a mixed system containing nitrobenzene (NB), benzoic acid (BA), and SMT based on previous studies [39,40], to further distinguish the relative contributions of the radicals and Fe(IV) on SMT degradation. The steady-state concentrations of •OH and $SO_4^{\bullet-}$ were calculated to be 0.64×10^{-15} and 6.33×10^{-15} M, using the reported second-order rate constants of the •OH, and $SO_4^{\bullet-}$ radicals toward NB, BA and SMT (Text S5), along with the experimental results in Fig. S9. Thus, the relative contribution of •OH, $SO_4^{\bullet-}$ and Fe(IV) in the Si-mZVI^{bm}/PDS system was estimated to be 7%, 53%, and 40%, consistent with that observed in the quenching experiments.

3.3. *Role of silicification in formation of reactive species*

It has been well-documented that ZVI-based catalysed persulfate activation occurs heterogeneously via direct electron transfer from the iron core to the persulfate and homogeneously through aqueous iron species (Eqs. 1–4) [9,13,15]. Therefore, understanding the effect of the silicification treatment on the electron transfer rate and the amount of ferrous ions released from ZVI-based catalysts can reveal the formation mechanism of the reactive species in Si-mZVI^{bm}/PDS.

$$Fe^0 + 2S_2O_8^{2-} \rightarrow Fe^{2+} + 2SO_4^{\bullet-} + 2SO_4^{2-} \quad (1)$$

$$Fe^{2+} + S_2O_8^{2-} + H_2O \rightarrow Fe^{IV}O^{2+} + 2H^+ + 2SO_4^{2-} \quad (2)$$

$$Fe^{2+} + S_2O_8^{2-} \rightarrow Fe^{3+} + SO_4^{\bullet-} + SO_4^{2-} \quad (3)$$

$$Fe^{3+} + S_2O_8^{2-} \rightarrow Fe^{2+} + S_2O_8^{\bullet-} \quad (4)$$

$$Fe^0 + 2H^+ \rightarrow Fe^{2+} + 2{\bullet}H \quad (5)$$

$${\bullet}H + S_2O_8^{2-} \rightarrow H^+ + SO_4^{\bullet-} + SO_4^{2-} \quad (6)$$

According to a more negative free corrosion potential corresponds to a faster electron transfer rate [22,41], the free corrosion potential of Si-mZVI^{bm} was determined as −0.830 V, which was more negative than that of mZVI^{bm} (−0.741 V) (Fig. 4(a)). Subsequently, the current densities generated by Si-mZVI^{bm} and mZVI^{bm} were calculated as 271.4 and 76.4 μA cm^{-2}, respectively. The electronic work function value for Si-mZVI^{bm} was significantly lower than that for mZVI^{bm} (Fig. S10(a)), revealing that electrons could more easily transfer through the oxide layer of Si-mZVI^{bm}. Moreover, Si-mZVI^{bm} presented a lower charge transfer resistance and more negative open circuit potential than mZVI^{bm} (Fig. S10(b) and (c)). Therefore, Si-mZVI^{bm} exhibited a higher electron transfer rate than mZVI^{bm}, suggesting that direct electron transfer from the iron core to PDS, producing $SO_4^{\bullet-}$, will enhance the degradation efficiency of Si-mZVI^{bm}/PDS process. The electron transfer rate of ZVI increased after silicification, which was primarily due to an increase in the electrical potential difference within the metal that formed a galvanic cell. Additionally, silicification promoted the adsorption of H_2O on ZVI (Fig. S11). The adsorbed H_2O (as a proton source) was quickly reduced to •H by the iron core, thereby accelerating the electron transfer and generation of $SO_4^{\bullet-}$ (Eqs. 5–6). EPR spectroscopy confirmed that more •H were generated over Si-mZVI^{bm} when 2,2,6,6,-tetramethylpiperidine-1-oxyl (TEMPO) was used as a trapping agent.

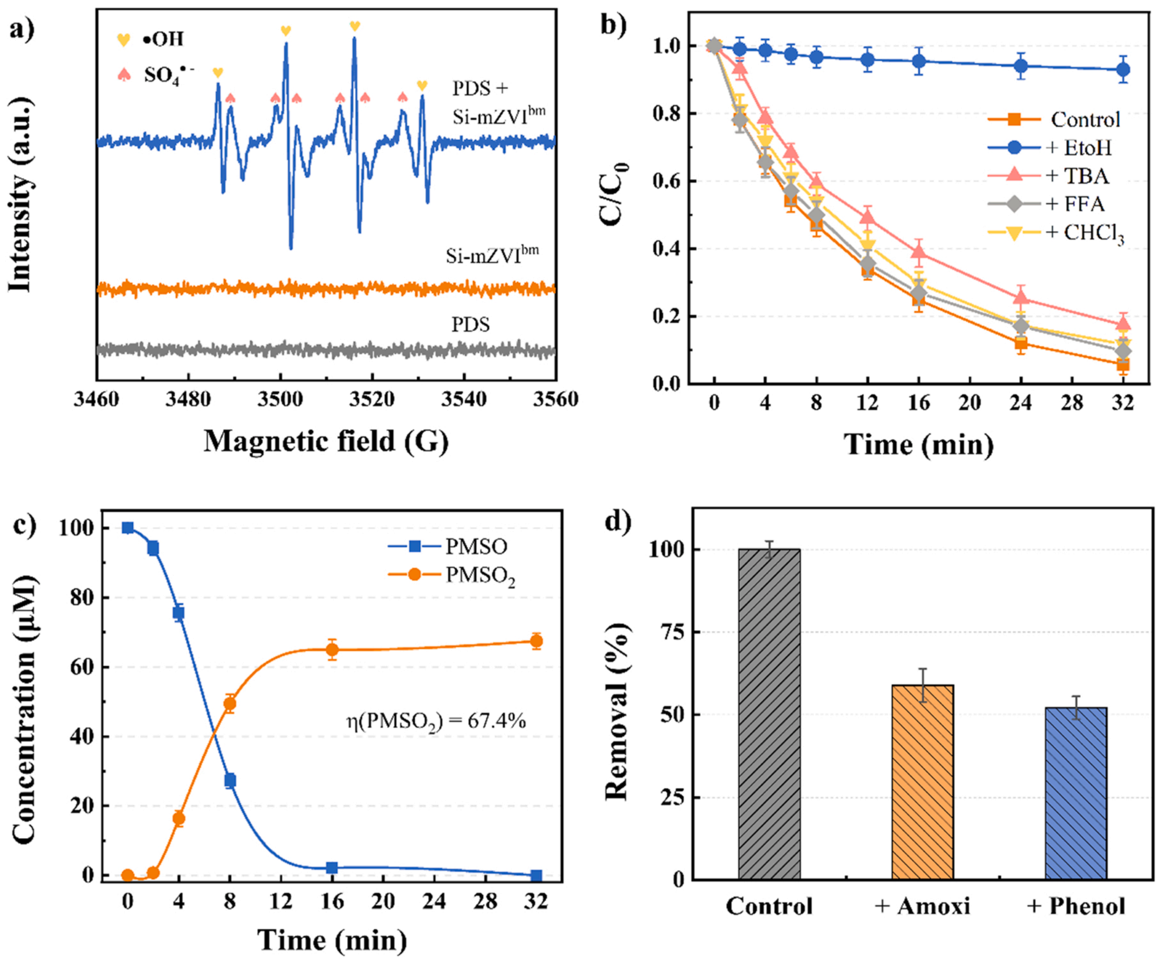

Fig. 3. (a) EPR spectra for •OH and $SO_4^{\bullet -}$ using DMPO as trapping agents (♠ represents the DMPO-SO_4^- adduct, ♥ represents the DMPO-OH adduct). (b) SMT degradation in the presence of EtOH (100 mM), TBA (100 mM), $CHCl_3$ (10 mM), and FFA (10 mM). (c) PMSO depletion and $PMSO_2$ generation in the Si-mZVI^{bm}/PDS system. (d) Effect of phenol (0.5 mM) and Amoxi (0.5 mM) on SMT removal in the Si-mZVI^{bm}/PDS process, reaction time of 30 min. Experimental conditions: 10 mg/L SMT, 100 μM PMSO, 0.15 g/L Si-mZVI^{bm}, 0.15 g/L mZVI^{bm}, 1.5 mM PDS and initial pH 7.5.

As shown in Fig. 4(b), Si-mZVI^{bm} induced a decrease in the three-line EPR signal intensity of TEMPO more quickly than mZVI^{bm}, further validating that more •H were generated over Si-mZVI^{bm}. These results indicate that silicification promoted the transfer of electrons from the iron core to PDS or H_2O, thereby accelerating the formation of $SO_4^{\bullet -}$ and Fe^{2+}.

Considering the important role of Fe^{2+} in the homogeneous activation of PDS, the amount of released Fe^{2+} was detected in the absence and presence of PDS. As expected, the concentration of total Fe dissolution of Si-mZVI^{bm} was higher than that of mZVI^{bm} in the absence of PDS (Fig. 4(c)), which agreed with the abovementioned corrosion potential analysis. The concentration of total iron in the presence of PDS (3.68 mg/L) was higher than that in the PDS-free (0.167 mg/L) solution, which can be attributed to the quick decrease in solution pH after the addition of PDS (Fig. S12), thus boosting the Fe dissolution [42]. It is noted that the Fe^{2+} concentration in Si-mZVI^{bm}/PDS system was significantly higher than that in mZVI^{bm}/PDS system, which could result from the quick corrosion of Fe^0 and more efficient redox cycles of Fe^{3+}/Fe^{2+} in Si-mZVI^{bm}/PDS system. Moreover, when 2,2-bipyridine (BPY) was introduced as a quenching agent for Fe^{2+}, SMT degradation was significantly suppressed (Fig. S13). These phenomena confirm that SMT degradation was related to the homogeneous Fe^{2+} and subsequent activation of PDS in the system.

In addition to silicification and supplied H^+, oxygen can promote Fe^{2+} production through the accelerated corrosion of Fe^0 (Eq. 7), and the generated Fe^{2+} could be released to the solution or absorbed on the ZVI surface [43–45]. More Fe^{2+} can be bound on the surface of Si-mZVI^{bm} due to the complexing effect of silicate on ferrous ions [32]. This is evidenced by the UV–vis spectra recorded in the presence of 1,10-phenanthroline (Fig. 4(d)) where a significant characteristic phenanthroline-Fe^{2+} peak at 510 nm appeared in the unfiltered Si-mZVI^{bm}/PDS, whereas the peak almost completely disappeared in the filtered reaction suspension. Previous studies suggested that ferrous ions bound on the iron oxide surface can chemically reduce dioxygen molecules to produce superoxide radicals ($O_2^{\bullet -}$) [46–48]. The redox potential of the Fe^{2+}/Fe^{3+} couple decreased when ferrous iron was coordinated by disilicate ions [31,49], thus providing an enhanced reducing capability for the ferrous ions to activate the dioxygen and lead to the generation of $O_2^{\bullet -}$ (Eqs. 8–9). The abovementioned mechanism was verified by EPR analysis (Fig. 4(e)), where stronger typical signals of the DMPO-O_2^- adducts were observed in the Si-mZVI^{bm}/PDS system, thereby confirming that silicification promoted the generation of $O_2^{\bullet -}$. The generation of $O_2^{\bullet -}$ might accelerate the redox cycles of Fe^{3+}/Fe^{2+} because $O_2^{\bullet -}$ can reduce ferric ions into ferrous ions (Eq. 10) ($k = 5 \times 10^7$ M^{-1} s^{-1} for $O_2^{\bullet -}$) [48]. Besides the reduction of ferric ions by $O_2^{\bullet -}$ and Fe^0, •H can also promote the regeneration of ferrous ions (Eqs. 11–12) [36,50]. These results could explain the long-lasting Fe^{2+} generation, which reacts with PDS to generate Fe(IV) or radicals (Eqs. 2–3).

$$2Fe^0 + 2\,H_2O + O_2 \rightarrow 2Fe^{2+} + 4OH^- \quad (7)$$

$$Fe^{2+} + \equiv silicate \rightarrow [\equiv silicate\text{-}Fe^{2+}] \quad (8)$$

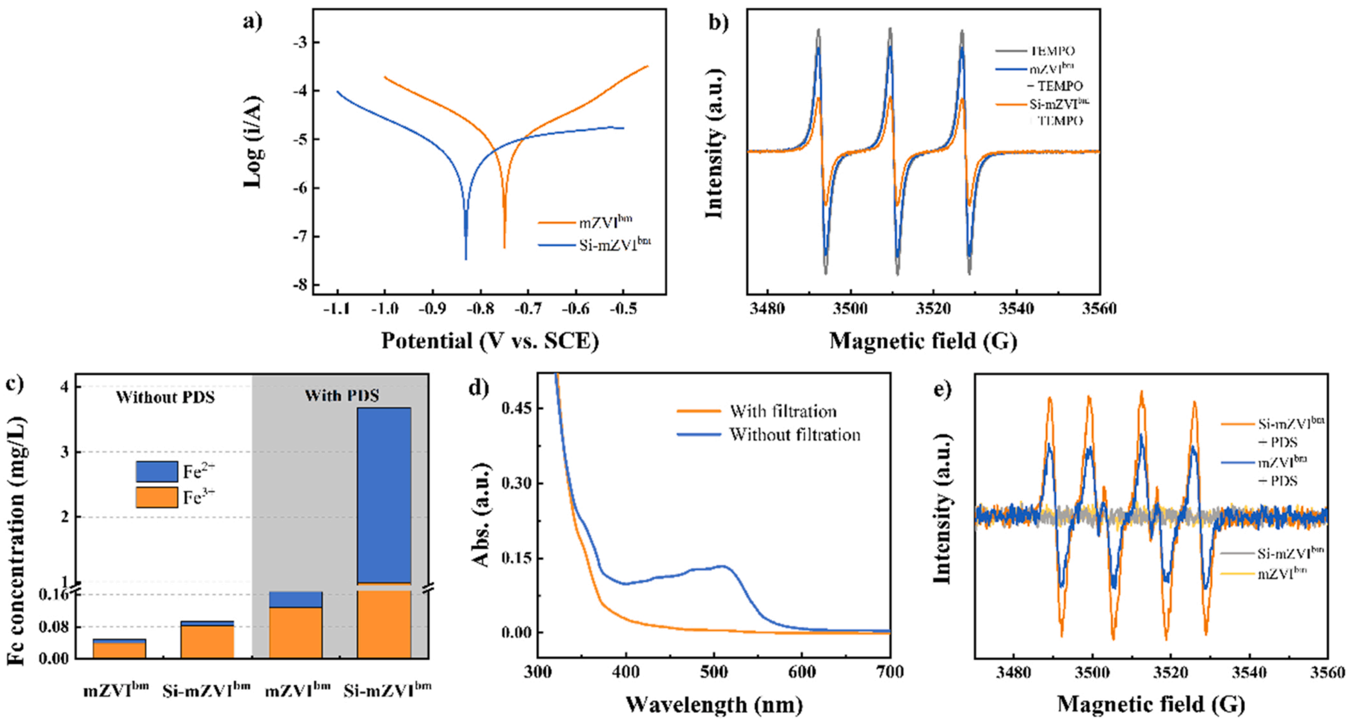

Fig. 4. (a) The Tafel profiles and (b) EPR spectra obtained from 25 mM TEMPO for 0 min, 25 mM TEMPO + 0.15 mg/mL^{-1} mZVI^{bm} for 10 min, and 25 mM TEMPO + 0.1 mg mL^{-1} Si-mZVI^{bm} for 10 min (c) The release of iron ions at different system. Experimental conditions: 10 mg/L SMT, 0.15 g/L Si-mZVI^{bm}, 1.5 mM PDS and initial pH 7.5. (d) UV–vis spectra of Si-mZVI^{bm}/PDS suspension and filtrate in the presence of phenanthroline. (e) EPR spectra for superoxide anion radical using DMPO as trapping agents.

$$[\equiv\text{silicate-Fe}^{2+}] + O_2 \rightarrow [\equiv\text{silicate-Fe}^{3+}] + O_2^{\bullet-} \tag{9}$$

$$O_2^{\bullet-} + Fe^{3+} \rightarrow O_2 + Fe^{2+} \tag{10}$$

$$Fe^0 + 2Fe^{3+} \rightarrow 3Fe^{2+} \tag{11}$$

$$\bullet H + Fe^{3+} \rightarrow H^+ + Fe^{2+} \tag{12}$$

3.4. Facilitation mechanism of silicification in the PDS activation process

$SO_4^{\bullet-}$, Fe(IV), and •OH were confirmed as the main reactive species for SMT removal in the Si-mZVI^{bm}/PDS system. Fig. 5 depicts the proposed facilitation mechanism for PDS activation and reactive species generation through the silicification treatment. The reactivity of ZVI-based catalysts is derived from the release of ferrous ions and its electron transfer capacity [6,12]. Unfortunately, the inherent passive iron oxide shell layer of bare ZVI limits the Fe^{2+} release through corrosion and inhibits electron transfer from the iron core to external, accounting for its low catalytic degradation performance.

Mechanical silicification of mZVI can significantly enhance the electron transfer capacity, and improve the efficiency of the activated PDS to produce $SO_4^{\bullet-}$ and Fe^{2+} by one-electron transfer (Stage I). Surface-bonded Fe^{2+} ($\equiv Fe^{2+}$) and •H are efficiently generated due to the galvanic corrosion of Si-mZVI^{bm} with the synergistic effect of the silicate-coated cathode, which further promotes the generation of $SO_4^{\bullet-}$ (Stage II). Concurrently, •OH may be generated through the oxidation of OH^- or H_2O by $SO_4^{\bullet-}$. The aqueous Fe^{2+} activates PDS to undergo a heterolytic O-O bond cleavage resulting in the formation of Fe(IV) (Stage III). The Fe^{2+} and Fe^{IV}=O are transformed into Fe^{3+} [39,51], and thus, a part of Fe^{3+} would be reduced into Fe^{2+} by Fe^0, •H, and $\bullet O_2^-$ (Stage IV). The rapid iron core oxidation and more efficient redox cycles of Fe^{3+}/Fe^{2+} contribute to sufficient solid/aqueous Fe^{2+} in the Si-mZVI^{bm}/PDS system, thereby resulting in the continuous production of active species.

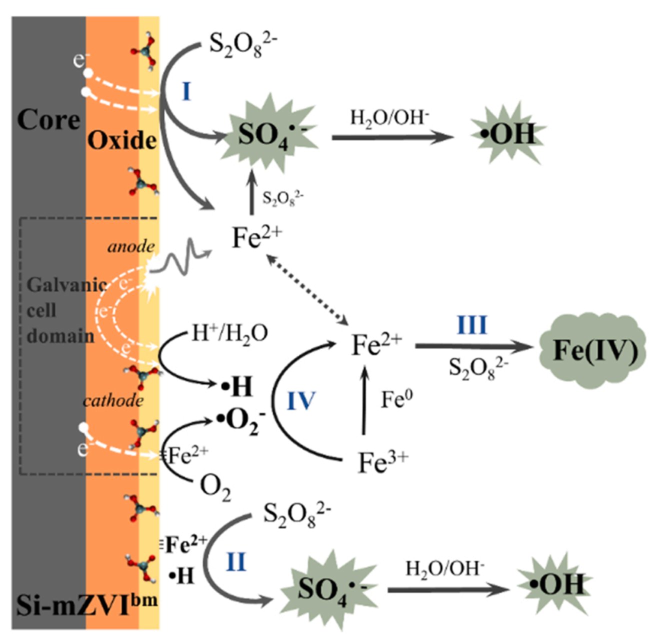

Fig. 5. A schematic of reaction mechanism PDS activation and reactive species generation in Si-mZVI^{bm}/PDS system.

The SEM analysis showed that only a few fragments were deposited on the surface of reacted mZVI^{bm}, and the reacted Si-mZVI^{bm} was covered with many small particles, some of which were irregularly clustered together (Fig. 6(a) and (b)). Meanwhile, the weight ratio of O element (28.61 wt%) on the surface of the reacted Si-mZVI^{bm} was higher than that of the reacted mZVI^{bm} (10.32 wt%). The iron oxide species of

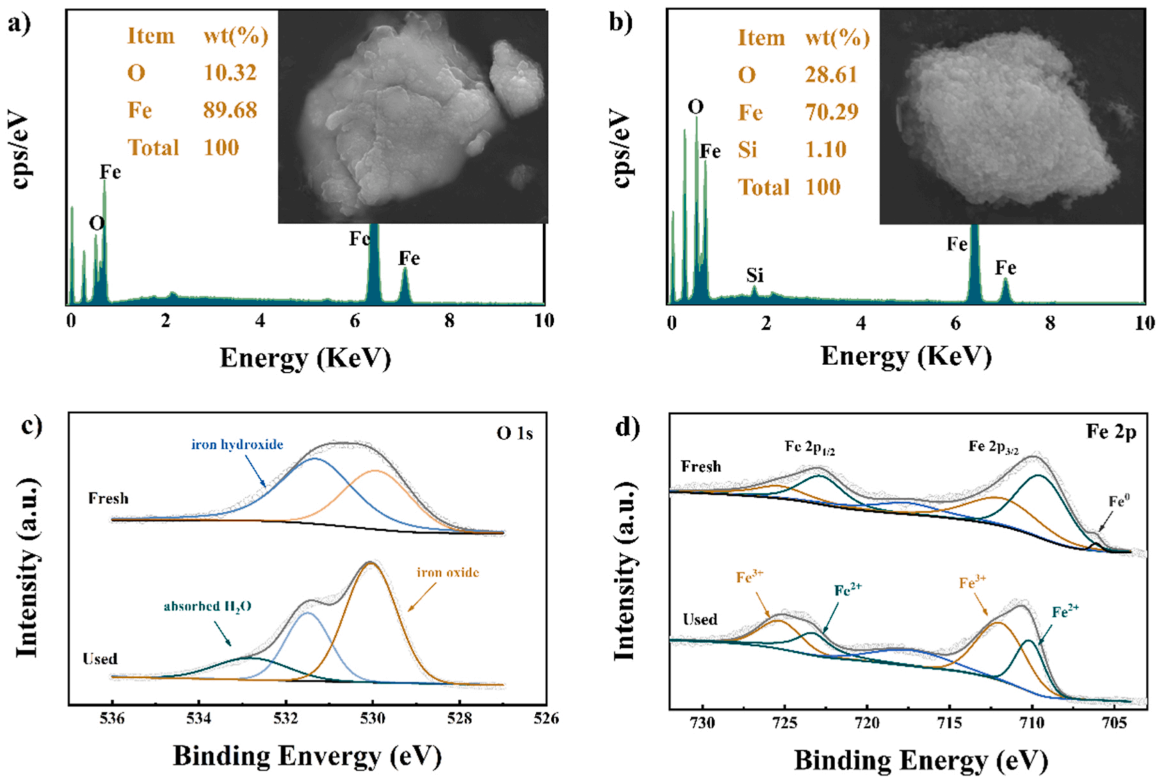

Fig. 6. SEM-EDX spectrum and morphology (inset) of reacted mZVI^{bm} (a) and Si-mZVI^{bm} (b) in the PDS activation process. XPS spectra of fresh and reacted Si-mZVI^{bm} particles in Si-mZVI^{bm}/PDS system (c) O 1s and (d) Fe 2p.

the reacted Si-mZVI^{bm} sample was further examined using XRD and Raman (Fig. S14(a) and (b)). The XRD diffraction peak of Fe^0 disappeared and the characteristic signals of iron oxide (Fe_2O_3, Fe_3O_4) and iron oxyhydroxide (FeOOH) appeared, indicating that the corrosion of Si-mZVI^{bm} was more rigorous than that of mZVI^{bm}. Raman spectroscopy confirmed that the iron corrosion products of Si-mZVI^{bm} after the persulfate-activating reaction primarily comprised Fe_2O_3 and γ-FeOOH with a small amount of Fe_3O_4. These results confirm that silicification accelerated the corrosion of ZVI in the presence of PDS.

XPS analysis was used to elucidate the surface chemical composition of the reacted mZVI^{bm} and Si-mZVI^{bm} samples for comparison. The broad peak of O 1 s was fitted by three peaks at the binding energy of 532.8, 531.3, and 530.0 eV, and were assigned to adsorbed H_2O, iron hydroxide, and iron oxide, respectively (Fig. 6(c)). The relative total content of iron oxide and adsorbed H_2O of the used Si-mZVI^{bm} particle were higher than before, demonstrating that iron oxide species were generated and the Si-mZVI^{bm} surface was strongly hydroxylated. The peaks at 725.3, 711.8, 723.3, 709.1, and 706.1 eV are assigned to Fe^{3+} $2p_{3/2}$, Fe^{3+} $2p_{1/2}$, Fe^{2+} $2p_{3/2}$ Fe^{2+} $2p_{1/2}$, and Fe^0 for Fe 2p, respectively (Fig. 6(d)). The characteristic Fe^0 peak of the used Si-mZVI^{bm} particle disappeared, and the proportion of Fe^{2+} decreased from 80.4% to 33.0%, confirming that Fe^0 and Fe^{2+} were oxidized in the catalytic reaction to produce iron oxides. Furthermore, high-resolution XPS depth profiles analyse (Fig. S15) indicted that the Fe^0 peak appeared in the reacted mZVI^{bm} sample with an increasing etch depth, whereas the Fe^0 signal was not observed in the Si-mZVI^{bm} sample, confirming that the iron core of Si-mZVI^{bm} was more severely consumed. With an increasing etching time, the Fe^{2+}/Fe_{total} molar ratio of the reacted Si-mZVI^{bm} was maintained above 65%, which was significantly higher than that of the reacted mZVI^{bm}, further demonstrating the more efficient redox cycles of Fe^{3+}/Fe^{2+} in the Si-mZVI^{bm}/PDS system.

Based on the total ion chromatograms and the mass spectrum acquired by HPLC-MS (Fig. S16), eight intermediates were deduced and their structural formulations and charge masses are depicted in Table S2. Fig. S17 shows the possible pathway of SMT degradation based on the results. SMT firstly undergoes hydroxylation of the aniline ring by Fe(VI) and electrophilic addition aromatic ring by •OH, forming hydroxyl-sulfamethazine (*m/z* 295 and 311) [39,52]. Thereafter, aromatic intermediates (*m/z* 226, 191 and 132) from the cleavage of the N-S bond of the SMT molecule following the $SO_4^{\bullet-}$ and Fe(IV) attack are formed [53]. Meanwhile, some products (*m/z* 200, 263 and 245) could generate by a Smiles-type rearrangement followed by SO_2 extrusion [52–54]. These results again indicated that Fe(IV) and radicals were generated in the Si-mZVI^{bm}/PDS system and contributed to the degradation of SMT.

3.5. Effect of key factors on the performance of Si-mZVI^{bm}/PDS

The degradation of SMT by the Si-mZVI^{bm}/PDS system showed a strong dependence on the initial pH value. Acidic and neutral pH conditions (pH 3.5–7.5) are more conducive to SMT degradation (Fig. S18). The highest k_{obs} of the Si-mZVI^{bm}/PDS system was observed at pH 3.5 (0.128 min^{-1}), which gradually decreased to 0.0012 min^{-1} when the pH increased to 11.5 (Fig. 7(a)). This higher degradation rate at a lower pH value was mainly due to the acidic condition that favors the formation of Fe^{2+} to catalyse the PDS activation to the generated reactive species (Eqs. 2–5). As the solution pH increased, the Fe^{2+} release began to decrease and the precipitation of aqueous Fe^{2+} and Fe^{3+} further limited the availability of Fe^{2+} [55,56]. The $SO_4^{\bullet-}$ was transformed to •OH through the reaction with H_2O or OH^- (Eqs. 13–14), while •OH at an alkaline pH had a lower redox potential [57]. Additionally, the oxidation power of aqueous Fe(IV) species decreased with an increasing pH [33], resulting in a lower SMT degradation efficiency.

$$SO_4^{\bullet-} + H_2O \rightarrow \bullet OH + SO_4^{2-} \tag{13}$$

$$SO_4^{\bullet-} + OH^- \rightarrow \bullet OH + SO_4^{2-} \tag{14}$$

The effect of PDS and Si-mZVI^{bm} as the main oxidant and catalyst for SMT degradation was investigated. As shown in Fig. 7(b), the

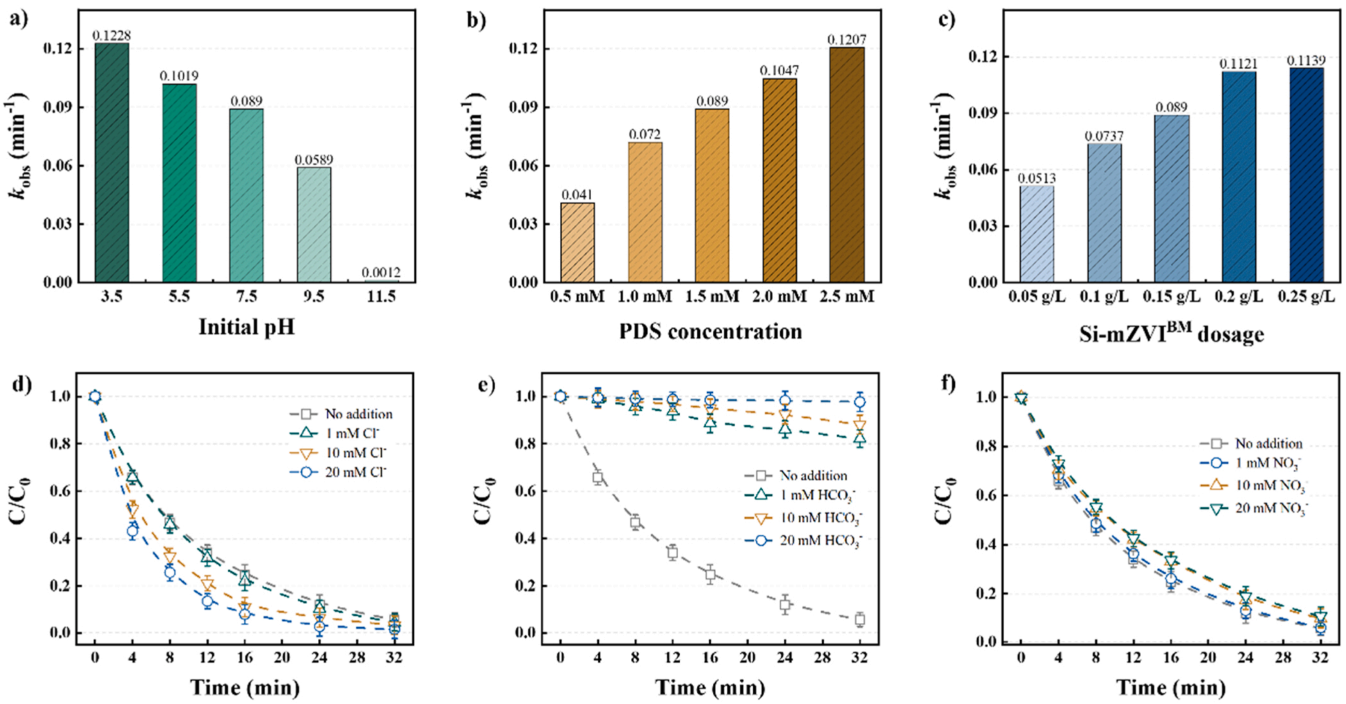

Fig. 7. The corresponding kinetic constants of the Si-mZVI^{bm}/PDS system under (a) different initial pH; (b) different PDS concentration; (c) different Si-mZVI^{bm} dosage. Effect of inorganic ions (d) Cl^-, (e) HCO_3^- and (f) NO_3^- on the SMT removal. Experimental conditions: 10 mg/L SMT, 0.15 g/L Si-mZVI^{bm} (Si/Fe = 0.04), 1.5 mM PDS and initial pH 7.5.

degradation rate increased considerably from 0.041 to 0.1207 min^{-1} when the PDS concentration was increased from 0.5 to 2.5 mM, because a higher PDS dosage facilitates the generation of reactive species [58], thus increasing SMT degradation. Fig. 7(c) shows the effects of different Si-mZVI^{bm} dosages on the degradation of SMT by Si-mZVI^{bm}/PDS. Increasing the Si-mZVI^{bm} dosage from 0.05 to 0.2 g/L, increased k_{obs} from 0.0513 to 0.1121 min^{-1}. Notably, when the Si-mZVI^{bm} dosage increased from 0.2 to 0.25 g/L, the SMT degradation improved only slightly. This phenomenon can be attributed to the highly reactive Si-mZVI^{bm}, which releases excess iron that could scavenge reactive intermediates (Eqs. 15–16) [11], and rapidly generate sulfate radical recombinations (Eq. 17) [37].

$$Fe^{2+} + SO_4^{\bullet -} \rightarrow SO_4^{2-} + Fe^{3+} \tag{15}$$

$$Fe^{2+} + 2\,H^+ + Fe^{IV}O^{2+} \rightarrow 2Fe^{3+} + H_2O \tag{16}$$

$$SO_4^{\bullet -} + SO_4^{\bullet -} \rightarrow S_2O_8^{2-} \tag{17}$$

$$Cl^- + SO_4^{\bullet -} \rightarrow SO_4^{2-} + Cl\bullet \tag{18}$$

$$Cl^- + \bullet OH \rightarrow OH^- + Cl\bullet \tag{19}$$

$$Cl^- + Cl\bullet \rightarrow Cl_2^{\bullet -} \tag{20}$$

$$HCO_3^- + \bullet OH \rightarrow H_2O + HCO_3^{\bullet} \tag{21}$$

$$HCO_3^- + SO_4^{\bullet -} \rightarrow SO_4^{2-} + HCO_3^{\bullet} \tag{22}$$

$$NO_3^- + SO_4^{\bullet -} \rightarrow SO_4^{2-} + NO_3^{\bullet} \tag{23}$$

$$NO_3^- + \bullet OH \rightarrow OH^- + NO_3^{\bullet} \tag{24}$$

Several inorganic anions widely exist in water environments and often interfere with catalytic reactions. Thus, the influence of different concentrations (1, 10, and 20 mM) of chloride (Cl^-), bicarbonate (HCO_3^-), and nitrate (NO_3^-) on SMT degradation in the Si-mZVI^{bm}/PDS system was examined. As shown in Fig. 7(d), the SMT degradation efficiencies improved with an increase in the Cl^- concentration. Generally, Cl^- can break the iron oxide layer and accelerate the pitting corrosion of ZVI to promote the release of Fe^{2+} [59]. Moreover, Cl^- can react with radicals to form sub-chlorinated radicals (Eqs. 18–20), thus promoting SMT degradation. Fig. 7(e) shows that the presence of HCO_3^- has an evident inhibitory impact on the degradation of SMT, which can be attributed to its scavenging effect on radicals (Eqs. 21–22), because the formed $HCO_3^{\bullet}$ is less active than $SO_4^{\bullet -}$ and •OH [60]. Additionally, the increase in pH caused by HCO_3^- adversely effected the degradation of SMT. NO_3^- had a relatively small effect on the SMT degradation (Fig. 7(f)), and a high concentration of NO_3^- could react with radicals to generate secondary free radicals, such as $NO_3^{\bullet}$ (Eqs. 23–24), which has difficulty in to removing SMT due to its weak oxidation capacity [2]. Overall, inorganic anions influence the order of the degradation degree of SMT as follows: $HCO_3^- > Cl^- > NO_3^-$.

4. Conclusions

An efficient PDS activator (Si-mZVI^{bm}) was synthesized through mechanical ball milling using mZVI and sodium disilicate as raw materials, and the degradation efficiency of SMT activated by Si-mZVI^{bm} under various conditions was clarified. Mechanical silicification effectively promoted the degradation rate of SMT in the Si-mZVI^{bm}/PDS system, as compared to unmodified mZVI. An increased in Si/Fe molar ratio from 1% to 8% resulted in an increase in the degradation rate. Fe (IV), •OH, and $SO_4^{\bullet -}$ were efficiently generated by PDS activation with Si-mZVI^{bm}, which resulted in the hydroxylation, N-S bond cleavage, and rearrangement degradation of SMT. The silicification treatment of mZVI accelerated the electron transfer rate, iron dissolution, and iron cycles, resulting in the continuous production of $SO_4^{\bullet -}$, •OH, and Fe(IV). The degradation of SMT was enhanced with an increase in the PDS (0.5–2.5 mM), and Si-mZVI^{bm} dosage (0.05–0.25 g/L), while it negatively relied on initial pH (3.5–11.5). The presence of inorganic ions ($HCO_3^- > Cl^- > NO_3^-$) significantly impacted the Si-mZVI^{bm}/PDS degradation of SMT. We believe that this study will facilitate the understanding of the effects of silicate modification on the catalytic reaction of iron-based persulfate processes, thereby providing high-efficiency ZVI-based technologies for water remediation.

CRediT authorship contribution statement

Minda Yu: Methodology, Validation, Investigation, Data curation, Writing – original draft, Funding acquisition. **Xuhui Mao:** Resource, Writing – review & editing Formal analysis. **Xiaosong He:** Investigation, Writing – review & editing. **Mingxia Zheng:** Validation, Methodology. **Xu Zhang:** Investigation, Methodology. **Jing Su:** Resource, Formal analysis. **Beidou Xi:** Supervision.

Declaration of Competing Interest

The authors declare that they have no known competing financial interests or personal relationships that could have appeared to influence the work reported in this paper.

Acknowledgements

The authors acknowledge the financial support the National Natural Science Foundation of China (42107070, 42030704), and the China Postdoctoral Science Foundation funded project (2020M680637, 2021T140636).

Appendix A. Supporting information

Supplementary data associated with this article can be found in the online version at doi:10.1016/j.apcatb.2022.121418.

References

[1] Q.-Q. Zhang, G.-G. Ying, C.-G. Pan, Y.-S. Liu, J.-L. Zhao, Comprehensive evaluation of antibiotics emission and fate in the river basins of China: source analysis, multimedia modeling, and linkage to bacterial resistance, Environ. Sci. Technol. 49 (2015) 6772–6782.

[2] W. Guo, Q. Zhao, J. Du, H. Wang, X. Li, N. Ren, Enhanced removal of sulfadiazine by sulfidated ZVI activated persulfate process: performance, mechanisms and degradation pathways, Chem. Eng. J. 388 (2020), 124303.

[3] B. Hong, S. Yu, Y. Niu, J. Ding, Q. Lin, X. Lin, W. Hu, Spectrum and environmental risks of residual pharmaceuticals in stream water with emphasis on its relation to epidemic infectious disease and anthropogenic activity in watershed, J. Hazard. Mater. 385 (2020), 121594.

[4] Y. Li, H. Dong, L. Li, J. Xiao, S. Xiao, Z. Jin, Efficient degradation of sulfamethazine via activation of percarbonate by chalcopyrite, Water Res. 202 (2021), 117451.

[5] Y.-G. Zhu, Y. Zhao, B. Li, C.-L. Huang, S.-Y. Zhang, S. Yu, Y.-S. Chen, T. Zhang, M. R. Gillings, J.-Q. Su, Continental-scale pollution of estuaries with antibiotic resistance genes, Nat. Microbiol. 2 (2017) 16270.

[6] H. Luo, Y. Zeng, D. He, X. Pan, Application of iron-based materials in heterogeneous advanced oxidation processes for wastewater treatment: a review, Chem. Eng. J. 407 (2021), 127191.

[7] H. Zhou, H. Zhang, Y. He, B. Huang, C. Zhou, G. Yao, B. Lai, Critical review of reductant-enhanced peroxide activation processes: Trade-off between accelerated Fe^{3+}/Fe^{2+} cycle and quenching reactions, Appl. Catal. B Environ. 286 (2021), 119900.

[8] Z. Wang, J. Jiang, S. Pang, Y. Zhou, C. Guan, Y. Gao, J. Li, Y. Yang, W. Qiu, C. Jiang, Is sulfate radical really generated from peroxydisulfate activated by iiiron (II) for environmental decontamination? Environ. Sci. Technol. 52 (2018) 11276–11284.

[9] Y. Zong, H. Zhang, X. Zhang, W. Liu, L. Xu, D. Wu, High-valent cobalt-oxo species triggers hydroxyl radical for collaborative environmental decontamination, Appl. Catal. B Environ. 300 (2022), 120722.

[10] Y. Zong, Y. Shao, Y. Zeng, B. Shao, L. Xu, Z. Zhao, W. Liu, D. Wu, Enhanced oxidation of organic contaminants by iron(II)-activated periodate: The significance of high-valent iron-oxo species, Environ. Sci. Technol. 55 (2021) 7634–7642.

[11] C. Kim, J.-Y. Ahn, T.Y. Kim, W.S. Shin, I. Hwang, Activation of persulfate by nanosized zero-valent iron (NZVI): Mechanisms and transformation products of NZVI, Environ. Sci. Technol. 52 (2018) 3625–3633.

[12] S. Xiao, M. Cheng, H. Zhong, Z. Liu, Y. Liu, X. Yang, Q. Liang, Iron-mediated activation of persulfate and peroxymonosulfate in both homogeneous and heterogeneous ways: a review, Chem. Eng. J. 384 (2020), 123265.

[13] J. Li, L. Yang, B. Lai, C. Liu, Y. He, G. Yao, N. Li, Recent progress on heterogeneous Fe-based materials induced persulfate activation for organics removal, Chem. Eng. J. 414 (2021), 128674.

[14] S. Rodriguez, L. Vasquez, D. Costa, A. Romero, A. Santos, Oxidation of orange G by persulfate activated by Fe(II), Fe(III) and zero valent iron (ZVI), Chemosphere 101 (2014) 86–92.

[15] J. Lee, U. von Gunten, J.-H. Kim, Persulfate-based advanced oxidation: Critical assessment of opportunities and roadblocks, Environ. Sci. Technol. 54 (2020) 3064–3081.

[16] Y. Hu, X. Peng, Z. Ai, F. Jia, L. Zhang, Liquid nitrogen activation of zero-valent iron and its enhanced Cr(VI) removal performance, Environ. Sci. Technol. 53 (2019) 8333–8341.

[17] Y.-G. Kang, S. Hong, H. Yoon, I.-G. Song, K. Cho, Y.-S. Chang, Mechanically combined persulfate on zerovalent iron: Mechanistic insights into reduction and oxidation processes, Chem. Eng. J. 414 (2021), 128772.

[18] Y. Xie, D.M. Cwiertny, Use of dithionite to extend the reactive lifetime of nanoscale zero-valent iron treatment systems, Environ. Sci. Technol. 44 (2010) 8649–8655.

[19] M. Li, Y. Mu, H. Shang, C. Mao, S. Cao, Z. Ai, L. Zhang, Phosphate modification enables high efficiency and electron selectivity of nZVI toward Cr(VI) removal, Appl. Catal. B Environ. 263 (2020), 118364.

[20] D. Fan, Y. Lan, P.G. Tratnyek, R.L. Johnson, J. Filip, D.M. O'Carroll, A. Nunez Garcia, A. Agrawal, Sulfidation of iron-based materials: a review of processes and implications for water treatment and remediation, Environ. Sci. Technol. 51 (2017) 13070–13085.

[21] J. Xu, A. Avellan, H. Li, X. Liu, V. Noël, Z. Lou, Y. Wang, R. Kaegi, G. Henkelman, G.V. Lowry, Sulfur loading and speciation control the hydrophobicity, electron transfer, reactivity, and selectivity of sulfidized nanoscale zerovalent iron, Adv. Mater. 32 (2020), 1906910.

[22] Y. Gu, B. Wang, F. He, M.J. Bradley, P.G. Tratnyek, Mechanochemically sulfidated microscale zero valent iron: Pathways, kinetics, mechanism, and efficiency of trichloroethylene dechlorination, Environ. Sci. Technol. 51 (2017) 12653–12662.

[23] F. Xu, S. Deng, J. Xu, W. Zhang, M. Wu, B. Wang, J. Huang, G. Yu, Highly active and stable Ni–Fe bimetal prepared by ball milling for catalytic hydrodechlorination of 4-chlorophenol, Environ. Sci. Technol. 46 (2012) 4576–4582.

[24] H. Lv, H. Niu, X. Zhao, Y. Cai, F. Wu, Carbon zero-valent iron materials possessing high-content fine Fe^0 nanoparticles with enhanced microelectrolysis-Fenton-like catalytic performance for water purification, Appl. Catal. B Environ. 286 (2021), 119940.

[25] A.N. Garcia, Y. Zhang, S. Ghoshal, F. He, D.M. O'Carroll, Recent advances in sulfidated zerovalent iron for contaminant transformation, Environ. Sci. Technol. 55 (2021) 8464–8483.

[26] V. Šepelák, M. Myndyk, M. Fabián, K.L.D. Silva, A. Feldhoff, D. Menzel, M. Ghafari, H. Hahn, P. Heitjans, K.D. Becker, Mechanosynthesis of nanocrystalline fayalite, Fe_2SiO_4, Chem. Commun. 48 (2012) 11121–11123.

[27] B. Li, B.F. Trueman, M.S. Rahman, Y. Gao, Y. Park, G.A. Gagnon, Understanding the impacts of sodium silicate on water quality and iron oxide particles, Environ. Sci. Water. Res. 5 (2019) 1360–1370.

[28] J.C. Rushing, L.S. McNeill, M. Edwards, Some effects of aqueous silica on the corrosion of iron, Water Res. 37 (2003) 1080–1090.

[29] A.L.-T. Pham, F.M. Doyle, D.L. Sedlak, Inhibitory effect of dissolved silica on H_2O_2 decomposition by iron(III) and manganese(IV) oxides: implications for H_2O_2-based in situ chemical oxidation, Environ. Sci. Technol. 46 (2012) 1055–1062.

[30] Z. Xiong, J. Li, Y. Li, Y. Yuan, Y. Jiang, G. Yao, B. Lai, Simultaneously enhanced degradation of N, N-dimethylacetamide and reduced formation of iron sludge by an efficient electrolysis catalyzed ozone process in the presence of dissolved silicate, J. Hazard. Mater. 406 (2021), 124725.

[31] M. Yu, J. Jia, X. Liu, J. Cui, B. Xi, X. He, X. Mao, *p*-Arsanilic acid degradation and arsenic immobilization by a disilicate-assisted iron/aluminum electrolysis process, Chem. Eng. J. 368 (2019) 428–437.

[32] J. Cui, X. Wang, K. Zheng, D. Wang, H. Zhu, X. Mao, Concentration-dependent enhancing effect of dissolved silicate on the oxidative degradation of sulfamethazine by zero-valent iron under aerobic condition, Environ. Sci. Technol. 54 (2020) 1242–1249.

[33] Z. Wang, W. Qiu, S. Pang, Y. Gao, Y. Zhou, Y. Cao, J. Jiang, Relative contribution of ferryl ion species (Fe(IV)) and sulfate radical formed in nanoscale zero valent iron activated peroxydisulfate and peroxymonosulfate processes, Water Res. 172 (2020), 115504.

[34] Y. Wu, X. Chen, Y. Han, D. Yue, X. Cao, Y. Zhao, X. Qian, Highly efficient utilization of nano-Fe(0) embedded in mesoporous carbon for activation of peroxydisulfate, Environ. Sci. Technol. 53 (2019) 9081–9090.

[35] J. Cui, L. Zhang, B. Xi, J. Zhang, X. Mao, Chemical oxidation of benzene and trichloroethylene by a combination of peroxymonosulfate and permanganate linked by in-situ generated colloidal/amorphous MnO_2, Chem. Eng. J. 313 (2017) 815–825.

[36] S. Deng, L. Liu, G. Cagnetta, J. Huang, G. Yu, Mechanochemically synthesized S-ZVI^{bm} composites for the activation of persulfate in the pH-independent degradation of atrazine: Effects of sulfur dose and ball-milling conditions, Chem. Eng. J. 423 (2021), 129789.

[37] Y. Li, X. Zhao, Y. Yan, J. Yan, Y. Pan, Y. Zhang, B. Lai, Enhanced sulfamethoxazole degradation by peroxymonosulfate activation with sulfide-modified microscale zero-valent iron (S-mFe^0): performance, mechanisms, and the role of sulfur species, Chem. Eng. J. 376 (2019), 121302.

[38] Y. Liu, H. Guo, Y. Zhang, W. Tang, X. Cheng, W. Li, Heterogeneous activation of peroxymonosulfate by sillenite $Bi_{25}FeO_{40}$: Singlet oxygen generation and degradation for aquatic levofloxacin, Chem. Eng. J. 343 (2018) 128–137.

[39] J. Liang, X. Duan, X. Xu, K. Chen, Y. Zhang, L. Zhao, H. Qiu, S. Wang, X. Cao, Persulfate oxidation of sulfamethoxazole by magnetic iron-char composites via nonradical pathways: Fe(IV) versus surface-mediated electron transfer, Environ. Sci. Technol. (2021).

[40] H. Dong, Y. Li, S. Wang, W. Liu, G. Zhou, Y. Xie, X. Guan, Both Fe(IV) and radicals are active oxidants in the Fe(II)/peroxydisulfate process, Environ. Sci. Technol. Lett. 7 (2020) 219–224.

[41] Y. Hu, G. Zhan, X. Peng, X. Liu, Z. Ai, F. Jia, S. Cao, F. Quan, W. Shen, L. Zhang, Enhanced Cr(VI) removal of zero-valent iron with high proton conductive $FeC_2O_4\cdot 2H_2O$ shell, Chem. Eng. J. 389 (2020), 124414.

[42] X. Li, S. Yang, M. Dzakpasu, S. Xu, D. Ding, G. Wang, R. Chen, P. Jin, X.C. Wang, Galvanic corrosion of zero-valent iron to intensify Fe^{2+} generation for peroxymonosulfate activation, Chem. Eng. J. 417 (2021), 128023.
[43] Q. Shao, C. Xu, Y. Wang, S. Huang, B. Zhang, L. Huang, D. Fan, P.G. Tratnyek, Dynamic interactions between sulfidated zerovalent iron and dissolved oxygen: mechanistic insights for enhanced chromate removal, Water Res. 135 (2018) 322–330.
[44] Y. Mu, Z. Ai, L. Zhang, F. Song, Insight into core-shell dependent anoxic Cr(VI) removal with Fe@Fe_2O_3 nanowires: Indispensable role of surface bound Fe(II), ACS Appl. Mater. Interfaces 7 (2015) 1997–2005.
[45] J. Qiao, Y. Guo, H. Dong, X. Guan, G. Zhou, Y. Sun, Activated peroxydisulfate by sulfidated zero-valent iron for enhanced organic micropollutants removal from water, Chem. Eng. J. 396 (2020), 125301.
[46] M.A. Voinov, J.O.S. Pagán, E. Morrison, T.I. Smirnova, A.I. Smirnov, Surface-mediated production of hydroxyl radicals as a mechanism of iron oxide nanoparticle biotoxicity, J. Am. Chem. Soc. 133 (2011) 35–41.
[47] Z. Ai, Z. Gao, L. Zhang, W. He, J.J. Yin, Core-shell structure dependent reactivity of Fe@Fe_2O_3 nanowires on aerobic degradation of 4-chlorophenol, Environ. Sci. Technol. 47 (2013) 5344–5352.
[48] J. Shi, Z. Ai, L. Zhang, Fe@Fe_2O_3 core-shell nanowires enhanced Fenton oxidation by accelerating the Fe(III)/Fe(II) cycles, Water Res. 59 (2014) 145–153.
[49] J. Cui, X. Wang, J. Zhang, X. Qiu, D. Wang, Y. Zhao, B. Xi, A.N. Alshawabkeh, X. Mao, Disilicate-assisted iron electrolysis for sequential Fenton-oxidation and coagulation of aqueous contaminants, Environ. Sci. Technol. 51 (2017) 8077–8084.
[50] H. Zeng, X. Zhao, F. Zhao, Y. Park, M. Sillanpää, Accelerated Fe^{3+}/Fe^{2+} cycle using atomic H* on Pd/Al_2O_3: A novel mechanism for an electrochemical system with particle electrode for iron sludge reduction in the Fe^{2+}/peroxydisulfate oxidation process, Chem. Eng. J. 382 (2020), 122972.
[51] H.-H. Kim, H. Lee, D. Lee, Y.-J. Ko, H. Woo, J. Lee, C. Lee, A.L.-T. Pham, Activation of hydrogen peroxide by a titanium oxide-supported iron catalyst: Evidence for surface Fe(IV) and its selectivity, Environ. Sci. Technol. 54 (2020) 15424–15432.
[52] L. Zhang, S. Shen, Adsorption and catalytic degradation of sulfamethazine by mesoporous carbon loaded nano zero valent iron, J. Ind. Eng. Chem. 83 (2020) 123–135.
[53] C. Kim, V.R. Panditi, P.R. Gardinali, R.S. Varma, H. Kim, V.K. Sharma, Ferrate promoted oxidative cleavage of sulfonamides: Kinetics and product formation under acidic conditions, Chem. Eng. J. 279 (2015) 307–316.
[54] X. Du, W. Fu, P. Su, J. Cai, M. Zhou, Internal-micro-electrolysis-enhanced heterogeneous electro-Fenton process catalyzed by Fe/Fe_3C@PC core-shell hybrid for sulfamethazine degradation, Chem. Eng. J. 398 (2020), 125681.
[55] H. Liu, J. Yao, L. Wang, X. Wang, R. Qu, Z. Wang, Effective degradation of fenitrothion by zero-valent iron powder (Fe^0) activated persulfate in aqueous solution: Kinetic study and product identification, Chem. Eng. J. 358 (2019) 1479–1488.
[56] I.M. Kolthoff, I.K. Miller, The chemistry of persulfate. I. The kinetics and mechanism of the decomposition of the persulfate ion in aqueous medium1, J. Am. Chem. Soc. 73 (1951) 3055–3059.
[57] G.P. Anipsitakis, D.D. Dionysiou, Radical generation by the interaction of transition metals with common oxidants, Environ. Sci. Technol. 38 (2004) 3705–3712.
[58] G. Barzegar, S. Jorfi, V. Zarezade, M. Khatebasreh, F. Mehdipour, F. Ghanbari, 4-Chlorophenol degradation using ultrasound/peroxymonosulfate/nanoscale zero valent iron: Reusability, identification of degradation intermediates and potential application for real wastewater, Chemosphere 201 (2018) 370–379.
[59] R. Hernandez, M. Zappi, C.-H. Kuo, Chloride effect on TNT degradation by zerovalent iron or zinc during water treatment, Environ. Sci. Technol. 38 (2004) 5157–5163.
[60] X. Zhang, X. Gu, S. Lu, Z. Miao, M. Xu, X. Fu, Z. Qiu, Q. Sui, Application of calcium peroxide activated with Fe(II)-EDDS complex in trichloroethylene degradation, Chemosphere 160 (2016) 1–6.